SAND REPORT

SAND2003-0245
Unlimited Release
Printed May 2003

Two-Dimensional CFD Calculations for YMP Natural Convection Tests

Nicholas D. Francis, Jr., Michael T. Itamura, Stephen W. Webb, and Darryl L. James

Prepared by
Sandia National Laboratories
Albuquerque, New Mexico 87185 and Livermore, California 94550

Sandia is a multiprogram laboratory operated by Sandia Corporation, a Lockheed Martin Company, for the United States Department of Energy under Contract DE-AC04-94AL85000.

Issued by Sandia National Laboratories, operated for the United States Department of Energy by Sandia Corporation.

Available to DOE and DOE contractors from
U.S. Department of Energy
Office of Scientific and Technical Information
P.O. Box 62
Oak Ridge, TN 37831

Telephone: (865)576-8401
Facsimile: (865)576-5728
E-Mail: reports@adonis.osti.gov
Online ordering: http://www.doe.gov/bridge

Available to the public from
U.S. Department of Commerce
National Technical Information Service
5285 Port Royal Rd
Springfield, VA 22161

Telephone: (800)553-6847
Facsimile: (703)605-6900
E-Mail: orders@ntis.fedworld.gov
Online order: http://www.ntis.gov/help/ordermethods.asp?loc=7-4-0#online

SAND2003-0245
Unlimited Release
Printed May 2003

Two-Dimensional CFD Calculations for YMP Natural Convection Tests

Nicholas D. Francis, Jr., and Michael T. Itamura
Subsystems Performance Assessment Department

Stephen W. Webb
Environmental Technology Department

Sandia National Laboratories
P.O. Box 5800
Albuquerque, NM 87185-0776

Darryl L. James
Texas Tech University
Department of Mechanical Engineering
Box 41021
Lubbock, TX 79409-1021

ABSTRACT

Processes important to the performance of a nuclear waste repository include cooling of spent nuclear fuel casks emplaced in tunnels bored into volcanic tuff. The geometry consists of an emplacement drift (tunnel), waste package, and a layer of gravel invert providing a flow barrier at the bottom of the drift. During the postclosure period, a drip shield, which is a thin metal sheet that covers the waste package, is also included. The geometry is in essence an enclosed annulus where the heated inner cylinder represents the waste package and the outer cylinder represents the emplacement drift. The waste package is below the centerline of the drift, so the geometry is eccentric. The invert floor impedes the flow in the lower portion of the annulus. Yucca Mountain Project (YMP) has developed two natural convection tests (25% and 44%-scale) in order to understand the heat transfer and fluid flow processes associated with this geometry. Measurements of temperature and fluid velocity are the primary results of the tests. Computational fluid dynamics (CFD) is used to determine the heating characteristics associated with the natural convection tests. The CFD analysis described in this report is two-dimensional. Steady-state annulus temperature distributions and flow fields are presented for different experimental heating conditions.

Maximum heat source temperatures from the CFD models range from 37°C to 50°C for cases without a drip shield and from 40°C to 56°C for cases with a drip shield. Hand calculations for a simplified geometry without a drip shield resulted in a temperature of 42.8°C for the 25%-scale configuration and 43.4°C for the 44%-scale configuration.

CONTENTS

FIGURES

Page

TABLES

Page

NOMENCLATURE

a	adsorption coefficient (m^{-1})
A_c	cross-sectional area (m^2)
c_p	specific heat (J/kg-K)
$c_{p,g}$	specific heat of invert grain (J/kg-K)
g	acceleration due to gravity (m/s^2)
H	drip shield height (m)
I	radiation intensity (W/m^2-solid angle)
k_{eq}	average equivalent thermal conductivity for natural convection (-)
k_a	air thermal conductivity (W/m-K)
l	cylinder length (m)
L	gap-width (m), $R_o - R_i$
L_c	characteristic gap-width (m)
M_w	molecular weight of air (kg/kmol)
n	refractive index
P	wetted perimeter (m)
Pr	Prandtl number (-)
Q_t	total heat transfer rate (W)
Q_c	the sum of convection and conduction heat transfer rates (W)
Q_r	radiation heat transfer rate (W)
$\vec{r}$	position vector (m)
R	drip shield radius (m)
R_g	universal gas constant (N-m/kmol-K)
Ra_L	Rayleigh number based on gap-width (-)
Ra_{L_c}	Rayleigh number based on characteristic gap-width (-)
R_o	outside radius (m)
R_i	inside radius (m)
$\vec{s}$	direction vector (m)
$\vec{s}'$	scattering direction vector (m)
T_i	inner concentric cylinder wall temperature (K or ^oC)
T_o	outer concentric cylinder wall temperature (K or ^oC)
DT	temperature difference (K or ^oC)

Greek

a	fluid thermal diffusivity (m^2/s)
b	volumetric thermal expansion coefficient (K^{-1})
ε	radiation emissivity
n	fluid kinematic viscosity (m^2/s)
r	fluid density (kg/m^3)
r_g	invert grain density (kg/m^3)
s_s	scattering coefficient (m^{-1})
s	Stefan-Boltzmann constant (W/m^2-K^4)
Φ	phase function
Ω'	solid angle (radians)

ACKNOWLEDGEMENTS

The authors would like to thank Teklu Hadgu of Sandia National Laboratories, and Sandra Dalvit-Dunn of Science and Engineering Associates, Inc., for their thorough reviews of this document. This work was supported by the Office of Repository Development as part of the Office of Civilian Radioactive Waste Management (OCRWM), which is managed by the U.S. Department of Energy, Office of Repository Development. Sandia is a multiprogram laboratory operated by Sandia Corporation, a Lockheed Martin Company, for the United States Department of Energy under Contract DE-AC04-94AL85000.

1 Introduction

This report illustrates an application of CFD modeling to an actual heating experiment in which internal natural convection and thermal radiation are the primary modes of heat transfer. The objective of this analysis is to develop two-dimensional steady-state CFD simulations for the 25%-scale and 44%-scale natural convection tests conducted at the Atlas Facility in Las Vegas, Nevada. Results of the experiments are described in detail in Sanchez and Howard, 2003. Comparison between models and data are to be performed in a future report. This report presents the results of the CFD models only.

The geometries described in this report are the same as the scaled geometries considered in the heat transfer analysis presented in Francis et al., 2003 (e.g., eccentric placement of the inner cylinder and a flow blockage below the inner cylinder with some cases including a drip shield). A schematic of the modeled geometry is shown in Figure 1. Hand calculations for a simplified geometry provide temperature predictions that supplement the use of CFD models. These calculations are presented in the Appendix of this report.

The CFD computer software code, FLUENT, version 6.0.12 (Fluent Incorporated, 2001), are used for this application. FLUENT is a computational fluid dynamics code that solves conservation of mass, momentum, energy (including a radiative transfer equation), species, and turbulence models (when applicable) using various means to obtain closure for the turbulent momentum equations. Transient or steady state formulations are also available with the code. Steady-state turbulent natural convection and thermal radiation are considered in this analysis.

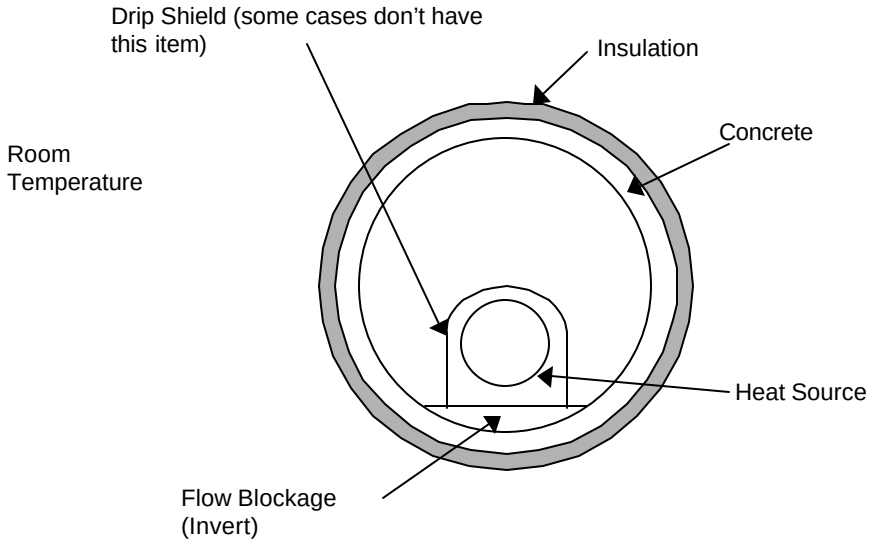

Figure 1. Schematic of the Experimental Test Set-Up.

2 Natural Convection Heat Transfer In The Literature

Previous experimental and theoretical studies of internal natural convection in the annulus between horizontal cylinders have been largely restricted to simple geometries such as concentric or eccentric cylinders. In many of these cases, the geometries have small (~ 3 cm) gap widths ($L = R_o - R_i$). Typically, a single radius ratio was considered (e.g., Kuehn and Goldstein, 1976a, considered a radius ratio of 2.6; Bishop, 1988, and McLeod and Bishop, 1989, considered a radius ratio of 3.37; Vafai et al., 1997, considered a radius ratio of 1.1). A limited number of numerical and experimental studies have investigated the influence of the radius ratio on internal flow characteristics (Lis, 1966; Bishop et al, 1968; Desai and Vafai, 1994; Char and Hsu, 1998). Some investigators developed heat transfer correlation equations for their experimental results (Lis, 1966; Bishop et al, 1968; Kuehn and Goldstein, 1976a and 1976b; Kuehn and Goldstein, 1978; Bishop, 1988). In the experimental studies, a range of radius ratios considered was $1.1 = R_o/R_i = 4$. In the numerical studies, a wider range of radius ratios was considered ($1.5 = R_o/R_i = 11$), including a radius ratio of 3.5, which is similar to that of the YMP geometry (Webb et al., 2002).

In the present report, interest is focused on large gap widths (on the order of 0.5 m or greater) and radius ratios ($R_o/R_i \sim 3.4$-3.5).

Most of the concentric and eccentric modeling studies consider gases (Pr ~ 0.7) as the working fluid in the annulus (Kuehn and Goldstein, 1976a; Kuehn and Goldstein, 1978; Farouk and Guceri, 1982; Desai and Vafai, 1994); although, some investigated a larger range of Prandtl numbers (Kuehn and Goldstein, 1976a; Desai and Vafai, 1994). A number of experimental analyses considered water (Pr ~ 5) as the working fluid in the annulus (Kuehn and Goldstein, 1976a). Some numerical studies considered Prandtl numbers as high as 5000 (engine oil at room temperature) and as low as about 0.01 (liquid metals).

The present study is for a gas with a Prandtl number of approximately 0.7 (e.g., dry air).

Table 1 lists the investigators and the forms in which their natural convection heat transfer investigations were presented (experiment, correlation equation, and numerical simulations).

Table 1. Internal Natural Convection Heat Transfer in the Literature

Investigators	Experimental Data	Correlation Equation	Numerical Simulation
Bishop, 1988	X	X	
Bishop et al., 1968	X	X	
Char and Hsu, 1998			X
Desai and Vafai, 1994			X
Farouk and Guceri, 1982			X
Fusegi and Farouk, 1986			X
Francis et al., 2002			X
Francis et al., 2003		X	X
Kuehn, 1976	X	X	X
Kuehn and Goldstein, 1976a	X	X	X
Kuehn and Goldstein, 1976b		X	
Kuehn and Goldstein, 1978	X	X	
J. Lis, 1966	X	X	
McLeod and Bishop, 1989	X	X	
Raithby and Hollands, 1975		X	X
Vafai et al., 1997	X	X	X
Webb et al., 2002	X		X

For internal natural convection in an annulus, a Rayleigh number based on gap-width

$$Ra_{L_c} = \frac{g\beta \Delta T L_c^{\,3}}{\nu \alpha} \tag{1}$$

is normally used to determine if the internal flow is laminar or turbulent (Kuehn and Goldstein, 1978). The Rayleigh number in equation (1) is based on a characteristic gap-width given by the following relationship:

$$L_c = \frac{2A_c}{P} \tag{2}$$

where A_c is the cross-sectional area of the flow domain and P is the wetted perimeter of the bounding walls. It is noted that equation (2) reduces to the standard gap-width definition, $L = R_o - R_i$, for a horizontal concentric cylinder annulus.

The transition gap-width Rayleigh number for turbulence is about 10^6 (Kuehn and Goldstein, 1978; Desai and Vafai, 1994; Char and Hsu, 1998). For Rayleigh numbers less than 10^6, the flow is laminar. For Rayleigh numbers greater than this transition value, the internal flow conditions for a heated inner cylinder are characterized by a turbulent upward moving plume above the inner heated cylinder and a turbulent downward flow against the cooled outer wall. Stagnation regions exist near the top where the plume impinges on the outer cylinder and over the entire bottom of the annulus. A low velocity core region exists in the annulus away from the walls.

The two-dimensional CFD models discussed in this report are developed for turbulent Rayleigh

numbers. The turbulent flow conditions are modeled using the two-equation renormalization group theory (RNG) *k-e* turbulence model as described in detail in Francis et al., (2002), for horizontal concentric cylinders of various size.

Turbulent flow conditions in an annulus are typically obtained either through the length scale (e.g., gap width) or the operating conditions (e.g., temperature difference and operating pressure) of the configuration. For the very small gap widths (~ 3 cm) considered in the experiments presented in the literature, air at atmospheric temperatures and pressures would not result in fully turbulent Rayleigh numbers (e.g., $Ra_L < 10^6$). Pressurized gases such as nitrogen were often used in experiments to obtain the fluid properties necessary to achieve turbulent Rayleigh numbers for very small gap widths and small temperature differences (Kuehn and Goldstein, 1978). The results of the experiments were then used to establish correlation equations that relate fluid properties and apparatus geometry to average heat transfer rates. Numerical models have been developed for some of the experimental geometries to compare model predictions to measured temperatures and heat transfer coefficients. Most of the numerical models are two-dimensional, but a limited number of three-dimensional studies have been conducted (Fusegi and Farouk, 1986; Desai and Vafai, 1994).

Most of the experimental data presented in the literature are restricted to heat transfer results such as temperature and equivalent thermal conductivity. Experimental measurements of fluid velocity and turbulence quantities have not been published in the literature for the horizontal concentric cylinder geometry.

3 CFD Models

An application of CFD modeling for natural convection heat transfer experiments is presented in this section. Both turbulent natural convection and thermal radiation are considered in the models. Two-dimensional CFD models using the RNG *k-e* turbulence model are used to estimate fluid velocities and component temperatures. The fluid flow, energy, and turbulence equations solved in this analysis are described in Francis et al., 2002. The radiative transfer equation (RTE) is described in Section 3.6 of this report.

CFD predictions for the 25%-scale and 44%-scale natural convection tests have been performed in conjunction with the development and operation of the natural convection tests to provide working guidance for expected operating conditions during the experiments. CFD model simulations described in this document are for both test configurations, in some cases including a drip shield. A schematic of the modeled test set-up is shown in Figure 1.

The simulations are performed with the information outlined in Table 2. The heat source and concrete pipe geometric data are obtained from Kalia (2001). The drip shield, insulation, and invert geometries are obtained from the test drawings (Natural Convection Test Assembly and Fabrication Detail Drawings, 2001). The heat source power requirements are obtained from Kalia (2001). Each test contains two heat source diameters. The smaller diameter heat source is selected for the CFD models because of its representation in the tests. (The smaller diameter heat sources make up at least 67% of the total number of heat sources in a given test.) Therefore, the 0.4 meter diameter heat source is selected for 25%-scale model and the 0.7 meter diameter heat

source is selected for the 44%-scale model. The power outputs for the 25%-scale models are 41 and 86.2 Watts. The power outputs for the 44%-scale models are 127 and 267.2 Watts. The 86.2 and 267.2 W heat sources represent the maximum power outputs from the variable spacing and power tests. The 41 and 127 W heat sources represent the maximum power outputs from the uniform spacing and power tests.

Refer to Table 2 for the entire suite of CFD simulations. The table provides the heat source, concrete pipe, and drip shield geometries (both radius and height). It also provides the power outputs (and heat flux) applied in the CFD simulations. It is noted that for the cases with a drip shield it is assumed that the drip shield thermal resistance is negligible. This simplification is considered reasonable since the drip shield is thin (0.25") and it has a large thermal conductivity.

Table 2. CFD Simulation Parameters

Case	Description	Heat Source Diameter (m)	Concrete Pipe Inner Diameter (m)	Drip Shield (m)	Power (W/package)	Heat Source Length (m)	Calculated Heat Flux[a] (W/m^2)
1	25%-scale, No drip shield, Uniform spacing and power	0.4	1.37	N/A	41	1.29	25.29
2	25%-scale, No drip shield, Variable spacing and power	0.4	1.37	N/A	86.2	1.29	53.18
3	25%-scale, With drip shield, Uniform spacing and power	0.4	1.37	R = 0.33 H = 0.305	41	1.29	25.29
4	25%-scale, With drip shield, Variable spacing and power	0.4	1.37	R = 0.33 H = 0.305	86.2	1.29	53.18
5	44%-scale, No drip shield, Uniform spacing and power	0.7	2.44	N/A	127	2.27	25.44
6	44%-scale, No drip shield, Variable spacing and power	0.7	2.44	N/A	267.2	2.27	53.53
7	44%-scale, With drip shield, Uniform spacing and power	0.7	2.44	R = 0.51 H = 0.61	127	2.27	25.44
8	44%-scale, With drip shield, Variable spacing and power	0.7	2.44	R = 0.51 H = 0.61	267.2	2.27	53.53

a – Used with a 1 m unit length in the models
N/A – Not Applicable

The concrete pipe and insulation thicknesses are 0.14 and 0.05 meters, respectively, for the 25%-scale natural convection tests and 0.25 and 0.05 meters, respectively, for the 44%-scale natural convection tests. As indicated in Figure 1, the heat source is eccentrically placed below the axis of the concrete pipe. The eccentricity is defined as the distance measured from the concrete pipe centerline to the heat source centerline. The eccentricity for the 25%-scale natural convection test is approximately 0.22 meters. The eccentricity for the 44%-scale natural convection test is approximately 0.43 meters.

Although the CFD simulations described in this report are two-dimensional and the actual test is three dimensional, this analysis should provide an overall idea of the operating conditions (temperatures and fluid velocities) for the chosen powers and geometries. Because the maximum heat source powers are used in these models, the results described in this report are expected to be hotter than the actual temperatures. Therefore, a more accurate description of the fluid flow and heat transfer between heat sources (and the end effects of individual heat sources) requires a three dimensional model. Detailed three-dimensional CFD models will be developed for both natural convection tests at a later date.

The following sections describe the development of the 2-D CFD simulations including specification of the geometries, input powers, thermal properties, operating conditions, boundary conditions, physical models, computational grids, and results.

3.1 Grids Used in the CFD Simulations

The computational grids used in the CFD simulations are illustrated for the 25%-scale geometry (44%-scale meshes are similar). Figure 2 illustrates the computational mesh for the model without a drip shield, Figure 3 illustrates the computational mesh for the model with a drip shield. Additional grid refinement in the near-wall regions is illustrated by an increased cell density near each of the walls. The increased cell density in the near-wall region is required by the turbulence model. The application of symmetry requires only half of the modeled domain. However, use of the symmetry boundary condition inherently assumes steady flow conditions in the annulus.

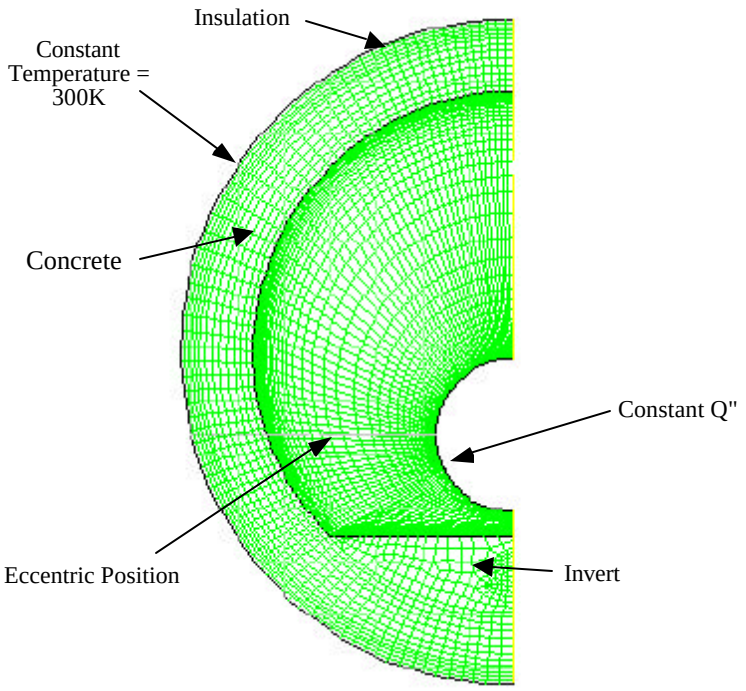

Figure 2. 25%-Scale Grid without Drip Shield.

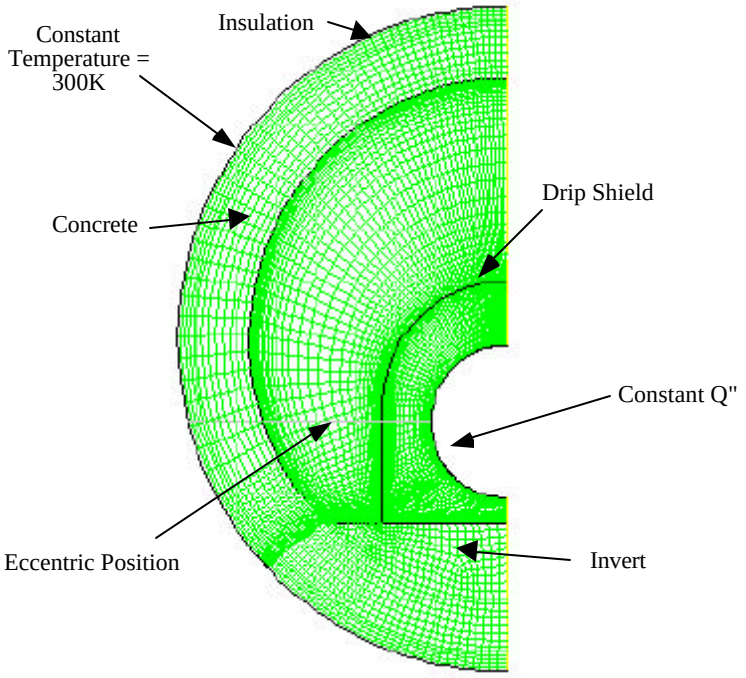

Figure 3. 25%-Scale Grid with Drip Shield.

3.2 Thermal Properties

CFD simulations require thermophysical properties of the introduced materials. The required properties include density, specific heat, thermal conductivity, and surface emissivity. Because the simulations provide steady state solutions, only the thermal conductivities and the emissivities affect the outcome of the final solutions. The simulations also require thermophysical properties for air, the working fluid within the annulus of the test apparatus. Table 3 provides the thermophysical properties of the introduced materials. Thermophysical properties of air are listed in Table 4.

Table 3. Thermophysical Properties of Introduced Materials[a]

Material	Density (kg/m^3)	Specific Heat (J/kg-K)	Thermal Conductivity (W/m-K)	Emissivity
Concrete	2280	1016	2.75	0.987
Stainless Steel (Drip Shield)	7950	445	16	0.828
Insulation	12	700	0.07	Not Required
Invert	2530	431	0.03	0.998
WP Steel (Heat Source)	7170	476	45	0.97

a – typical YMP material properties associated with the natural convection tests

The thermal properties given in Table 3 are average values. The dependence of introduced material thermal properties on temperature is small in the range of test operation.

The density and the specific heat for the porous invert material is obtained from the following equation (note that a 0% moisture content is used in the invert and the thermal capacitance ($\rho_a c_{p,a}$) of air is much smaller than that of the invert):

$$\left(\rho c_p\right)_s = \rho_g (1-\phi) c_{p,g} + \phi \rho_a c_{p,a} \approx \rho_g (1-\phi) c_{p,g} \qquad (3)$$

where ρ_g (=2530 kg/m^3), $c_{p,g}$ (=948 J/kg-K), and ϕ (= 0.545). Each of these invert properties has been used in the past by YMP. Maintaining a solid density of 2530 kg/m^3, an effective specific heat is computed using equation (3) as 431 J/kg-K. Therefore, the invert material is treated in this analysis as a solid material with a thermal capacitance of 1.09×10^6 J/m^3-K. However, for steady-state solutions, the thermal capacitance does not influence the final solutions.

Table 4. Thermophysical Properties for Air[a]

Temperature (K)	Density[b] (kg/m^3)	Specific Heat (J/kg-K)	Thermal Conductivity (W/m-K)	Viscosity (kg/s-m)
300	Incompressible-ideal-gas	1007	0.0263	$1.846x10^{-5}$
350	Incompressible-ideal-gas	1009	0.03	$2.082x10^{-5}$

a- Incropera and DeWitt, 1990
b- Described in section 3.2.1

Air thermal properties are given at two temperatures (Incropera and DeWitt, 1990). They are evaluated in a piecewise-linear solution (in terms of the temperature) directly in the model. Thermal radiation properties are not supplied for the air because an assumption is made that the air does not participate in the thermal radiation heat transfer occurring in the annulus. This assumption is reasonable for low relative humidities.

3.2.1 Incompressible ideal gas

For all of the cases considered in the report, the dynamic viscosity, thermal conductivity, and specific heat of air are all inputs in the simulations as given in Table 4. The fluid density is computed by FLUENT using the incompressible-ideal-gas law. The incompressible-ideal-gas law is

$$r = \frac{P_o}{\frac{R_g}{M_w}T} \tag{4}$$

where P_o is the operating pressure described in the next section and T is the fluid temperature.

Internal natural convection occurs when a density variation (due to a temperature gradient) exists in a gravitational field. The incompressible-ideal-gas law is used (by FLUENT) when pressure variations are small enough such that the overall internal flow conditions are essentially incompressible, but a relationship between density and temperature is required since this is the driving force for flow (buoyancy). From equation (4) it is noted that the internal density variation is based on the input ambient operating pressure and the computed temperature.

3.3 Operating Conditions

The approximate ambient operating pressure at the Atlas Facility in Las Vegas, Nevada is approximately 94,400 Pa (Nevada Bureau of Mines and Geology, www.nbmg.unr.edu), standard atmospheric pressure at just less than 2,000 feet elevation (600 meters above sea level). The acceleration due to gravity applied in the simulations is assumed to be 9.81 m/s^2.

3.4 Boundary Conditions

Calculated surface heat fluxes are given in Table 2 for each case. A uniform surface heat flux is assumed for the inner cylinder. The cylinder wall is stationary and the no-slip fluid flow condition is enforced at the surface. For the cases with a drip shield present, the drip shield wall is impermeable and stationary and the no-slip fluid flow condition is enforced on both sides. A no-slip fluid flow condition is enforced on the inside surface of the concrete pipe and the top surface of the invert floor. Finally, the outer insulation surface is specified as a uniform temperature boundary at 300K (26.9^{o}C). All solid surfaces within the annulus participate in thermal radiation. Surface emissivities are given in Table 3.

3.5 CFD Model Settings and Parameters

The CFD model settings and runtime monitoring for equation residuals, discretization, convergence, and steady-state energy balance are described in this section.

FLUENT uses a control-volume method to solve the governing equations. The equations are discrete for each computational cell. In using this solution method the CFD model stores flow properties (e.g., dependent variables) at the cell centers. However, face values are required for the convection terms in the discretized equations. Face values are obtained by interpolation from the cell centers using a second-order upwind scheme for the momentum and energy equations and a first-order upwind scheme for the turbulence equations. It is noted that the diffusion terms in the equations are central-differenced and are second-order accurate. The PRESTO! (PREssure Staggering Option) pressure interpolation scheme is applied to this analysis to compute face pressure from cell center values. Pressure-velocity coupling is achieved through the SIMPLE algorithm. The SIMPLE (Semi-Implicit Method for Pressure-Linked Equations) algorithm uses the discrete continuity equation to determine a cell pressure correction equation. Once a solution to the cell pressure correction equation is obtained the cell pressure and face mass fluxes are then corrected using the cell pressure correction term.

Because the equation set being solved is linearized, it is necessary to control the rate of change of the flow/energy variables at each iteration step. Under-relaxation parameters are assigned to pressure, momentum, energy, turbulence kinetic energy, turbulence dissipation rate, and a variety of others that go unmodified from default settings (usually 1.0). For the buoyancy driven flow problems considered in this report, the default settings for the under-relaxation parameters for the flow equations are too high. Therefore, additional under-relaxation is necessary to obtain a converged solution. Typically, the flow equation (momentum, turbulent kinetic energy, and dissipation rate of turbulent kinetic energy) underrelaxation parameters are set at about 0.15 to 0.2.

A flow solution is considered to have converged after all equation residuals have been reduced by about 4 to 5 orders of magnitude. For the higher Rayleigh number flow cases, this may require about 10,000 or more iterations to achieve. A final convergence criteria specified in the CFD simulations is based on an overall steady-state energy balance. When the energy imbalance is at or below about 1-2%, the flow simulation is assumed to be at steady-state.

3.6 Physical Models

3.6.1 Turbulence Model

Based on the calculations given in Appendix A and considering the test geometries and temperatures (e.g., large gap widths with temperature differences of about 5°C or more between components), turbulent flow conditions are expected in the test annuli. Therefore, turbulence transport equations are required in the solution of the governing conservation equations (e.g., mass continuity, Reynolds-Averaged Navier-Stokes, and thermal energy (including thermal radiation)). The RNG *k-e* turbulence model is selected for the simulations. This turbulence model uses a differential viscosity model to account for viscosity effects in the near-wall region. Subsequently, the laminar sublayer in the near-wall region must be appropriately resolved by the grid. Refer to grid considerations in Sections 3.1 and 3.7.1. The (RNG) *k-e* turbulence model is one of a number of different models available for use in FLUENT as described in detail in Section 2.2 of Francis et al., 2002.

3.6.2 Thermal Radiation

The thermal radiation model used in this CFD analysis is based on the radiative transfer equation (RTE)

$$\nabla \cdot \left(I(\vec{r},\vec{s})\vec{s}\right) + (a + s_s) I(\vec{r},\vec{s}) = an^2 \frac{s\,T^4}{p} + \frac{s_s}{4p} \int_0^{4p} I(\vec{r},\vec{s}') \Phi(\vec{s}\cdot\vec{s}')\, d\Omega' \qquad (5)$$

Thermal radiation heat transfer is accounted for by solving equation (5) using the discrete ordinates (DO) model included as an option in FLUENT (refer to the FLUENT Users Manual, 2001, Chapter 11, Modeling Heat Transfer). The DO model solves the RTE for a finite number of discrete solid angles (called control angles). Division of a domain occurs as N_q *x* N_f solid angles. In two-dimensional calculations, four octants are required making a total of $4N_qN_f$ directions solved, one RTE for each direction. Control angles are further subdivided into N_{qp} *x* N_{fp} pixels, in order to account for the possibility of incoming and outgoing radiation occurring within the same control angle. The DO model allows one to solve surface-to-surface radiation and fluid participation radiation. This model is restricted to either gray or non-gray thermal radiation using a banded gray model. The RTE accounts for scattering, gas emission, and adsorption; however, in these simulations, the air inside the annulus is treated as a non-participating fluid. The surfaces are treated as gray, diffuse surfaces.

The DO settings used in these simulations are theta divisions (=6), phi divisions (=6), theta pixels (=6), and phi pixels (=6). This results in the solution of 144 RTEs at each radiation iteration. The number of flow iterations per radiation iteration is the default value of 10. The default gray radiation model is applied as a constant emissivity over all wavelengths. Since the air is treated as non-participating, the adsorption, scattering, and refractive index coefficients for thermal radiation are 0 m^{-1}, 0 m^{-1}, and 1, respectively.

3.6.3 Thermal Conduction

Thermal conduction is the sole mode of heat transfer in the concrete, invert, and insulation. Each is treated as a solid media; therefore, no convection or thermal radiation is calculated in those media.

3.7 Results of the CFD Application

The CFD simulations provide component temperatures and fluid velocities. Table 5 indicates the maximum heat source temperature as well as area weighted wall temperatures for the heat source, drip shield (if included), inside concrete pipe, and invert (both inside and outside the drip shield, if present). A description of the test layout is provided in Table 5 in order to associate a model with a particular test. Additionally, the power is listed in the table as a quick reference guide to a particular heat source in a given test. The heat flux boundary conditions indicated in Table 2 and applied in the models are based on these powers.

Table 5. Two-Dimensional CFD Predicted Temperatures

Case	Description	Power (W)	Average Fluid Temp.[a] (°C) Inside, Outside Drip Shield	Heat Source Maximum Temp. (°C)	Average Heat Source Temp. (°C)	Average Inner Concrete Surface Temp. (°C)	Average Invert Temp. (°C) Inside, Outside Drip Shield	Average Drip Shield Temp. (°C)
1	25%-scale, No drip shield, Uniform spacing and power	41	33.6	37.3	36.1	32.2	33.7	N/A
2	25%-scale, No drip shield, Variable spacing and power	86.2	40.7	47.5	45.5	38.0	40.9	N/A
3	25%-scale, With drip shield, Uniform spacing and power	41	36.9, 33.4	40.2	39.2	32.2	37.07, 32.7	35.0
4	25%-scale, With drip shield, Variable spacing and power	86.2	47.1, 40.4	53.1	51.3	38.0	47.3, 38.9	43.5
5	44%-scale, No drip shield, Uniform spacing and power	127	34.1	38.4	36.8	32.6	34.5	N/A
6	44%-scale, No drip shield, Variable spacing and power	267.2	41.7	49.8	46.9	39.0	42.5	N/A
7	44%-scale, With drip shield, Uniform spacing and power	127	37.9, 33.8	41.8	40.1	32.6	38.5, 33.3	35.7
8	44%-scale, With drip shield, Variable spacing and power	267.2	48.9, 41.3	56.2	53.2	39.0	50.1, 40.3	44.8

a – An average fluid temperature obtained from the eccentric position for both the with and without drip shield cases (for cases with a drip shield, the first value is the inside fluid temperature while the second value is the outside fluid temperature)

With these estimates, one can assess the operation of both natural convection tests. Recall, however, that the CFD simulation results presented in this report are *two-dimensional*. Therefore, one may expect that the models may be hotter than the actual temperature measurements (in particular for the 86.2 W and 267.2 W cases because these originate from the distributed tests; the 41 W and 127 W cases may not be as far off from their three-dimensional counterparts because they originate from the uniform tests).

Temperature contours and velocity vectors (in terms of velocity magnitude) are shown at steady state for a number of the simulations. As expected, the 44%-scale simulations have higher Rayleigh numbers and hence higher fluid velocities. For quick reference in the upcoming figures, the left facing results are from the 25%-scale simulations; the right facing results are from the 44%-scale simulations.

Temperature contours and velocity vectors are shown in Figures 4 and 5 for the 86.2 W, 25%-scale, drip shield case. The temperature contours indicate the traditional flow pattern for internal natural convection in an annulus. An upward moving heated plume is evident both inside and outside the drip shield. The heated plume separates from the inner surface and impinges on the top surface (e.g., flow separates from the inner heated cylinder and impinges on the top of the drip shield for inside flow, flow separates from the outside surface of the drip shield and impinges on the top of the concrete pipe for outside flow). Descending air flows along an outside wall cooling as it moves towards the invert floor. The air is heated as it returns to the inner surfaces and the process repeats itself. Thermal radiation underneath the drip shield heats the invert floor beneath the heat source.

The velocity vectors also indicate this typical buoyant flow pattern. Note that the velocity vector lengths shown in Figure 5 are greatly exaggerated in order to illustrate the general direction of flow both inside and outside the drip shield. Upward moving flow adjacent to the heat source separates off the top of the inner cylinder. The upward moving fluid then impinges on the top of the drip shield and descends along the drip shield inner surface, cooling as it descends. The air is reheated and the process repeats itself. The flow pattern outside the drip shield is similar, heated air moving upward along the outside surface of the drip shield impinges on the top of the concrete pipe then it descends (while cooling) along the concrete wall towards the invert floor where the process repeats itself. The upward moving plumes and descending flows are turbulent.

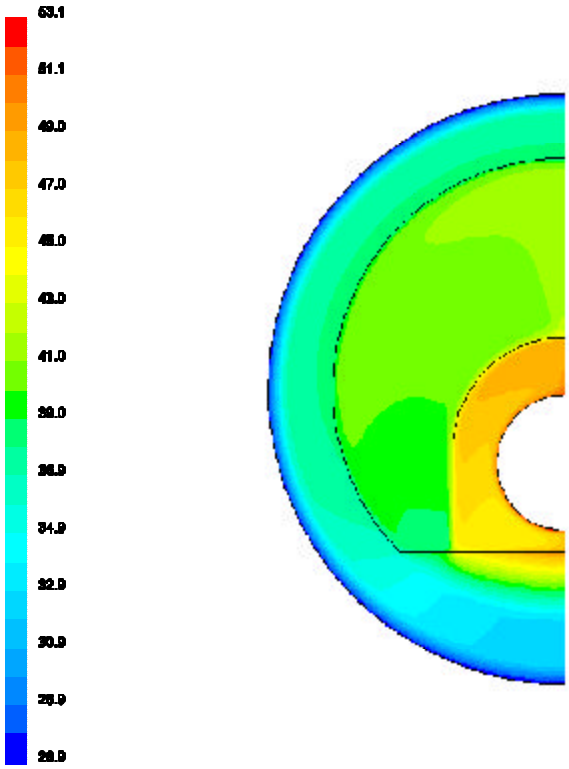

Figure 4. Temperature Contours (^{o}C) at Steady State for the 86.2 W Case (25%-scale, with Drip Shield).

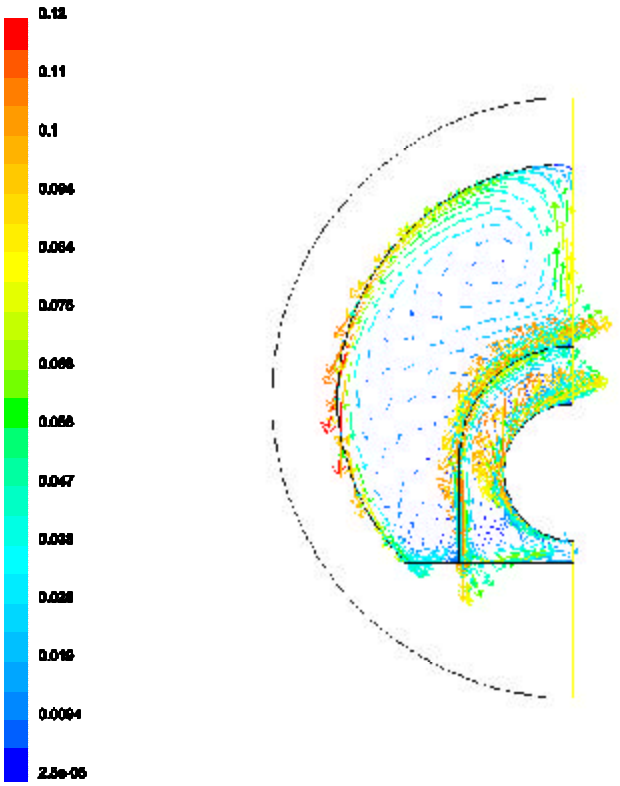

Figure 5. Velocity Vectors (m/s) at Steady State for the 86.2 W Case (25%-scale with Drip Shield).

Temperature contours and velocity vectors are shown in Figures 6 and 7 for the 267.2 W, 44%-scale, drip shield case. Although at a larger scale, the internal flow pattern is identical to the previous case. The heat source temperatures are slightly higher than the previous case. The air velocities are higher as expected for the larger Rayleigh numbers.

As noted from Figures 5 and 7, the core region of the modeled domain contains a very slow moving fluid. (Again, note the two-dimensional assumption. In three dimensions, this core fluid has an axial component of velocity.)

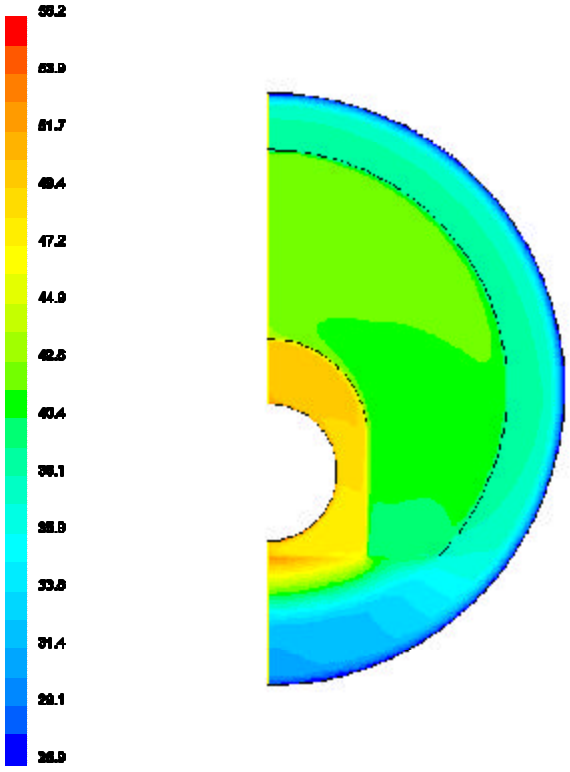

Figure 6. Temperature Contours (^{0}C) at Steady State for the 267.2 W Case (44%-scale with Drip Shield).

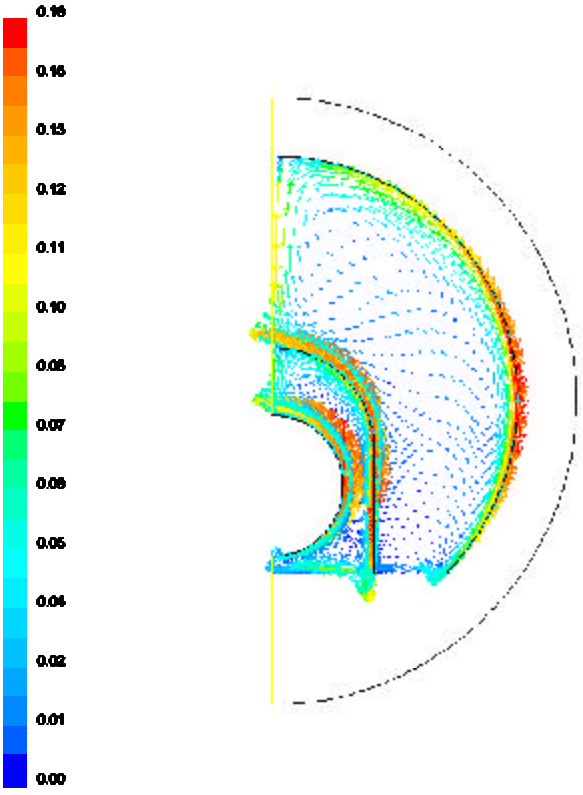

Figure 7. Velocity Vectors (m/s) at Steady State for the 267.2 W Case (44%-scale with Drip Shield).

Figures 8-11 illustrate the same cases without the drip shield. Subsequently, heat transfer and fluid flow occurs directly across a much larger gap. This being the case, it is expected that the fluid velocities would be higher and the temperatures would be different when compared to the drip shield simulations.

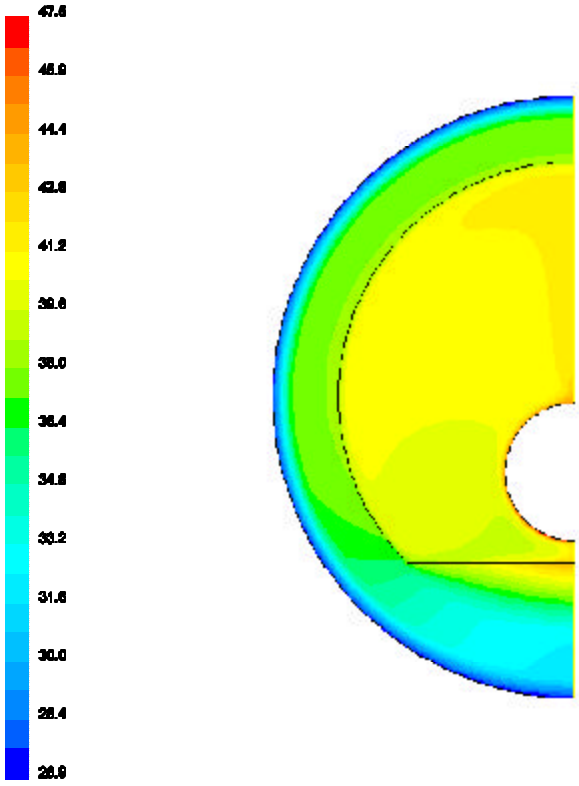

Figure 8. Temperature Contours (°C) at Steady State for the 86.2 W Case (25%-scale without Drip Shield).

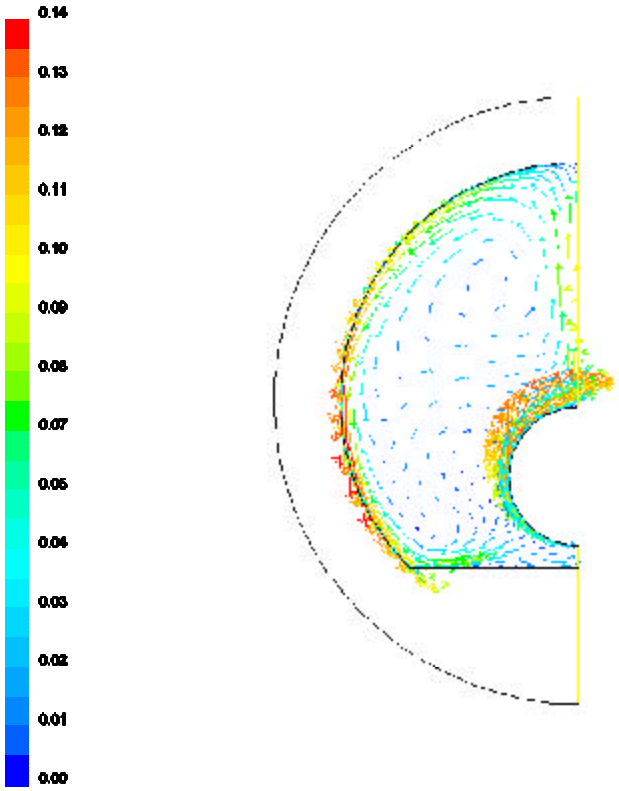

Figure 9. Velocity Vectors (m/s) at Steady State for the 86.2 W Case (25%-scale without Drip Shield).

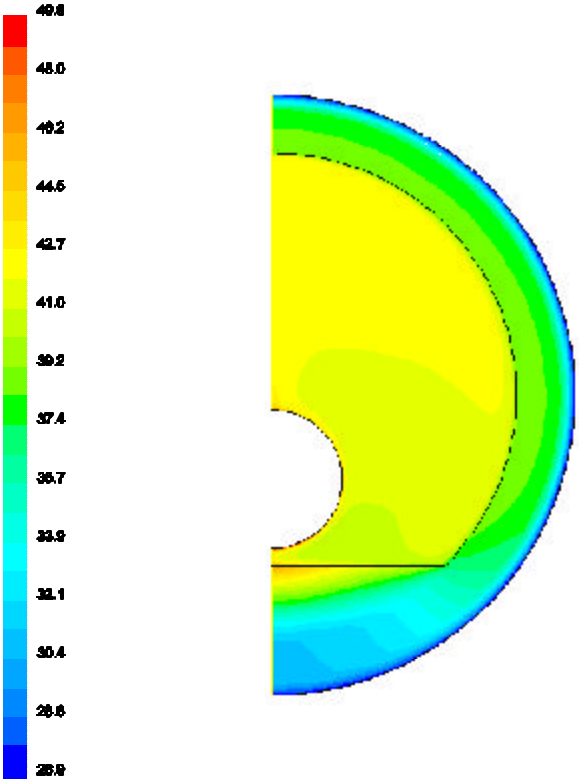

Figure 10. Temperature Contours (°C) at Steady State for the 267.2 W Case (44%-scale without Drip Shield).

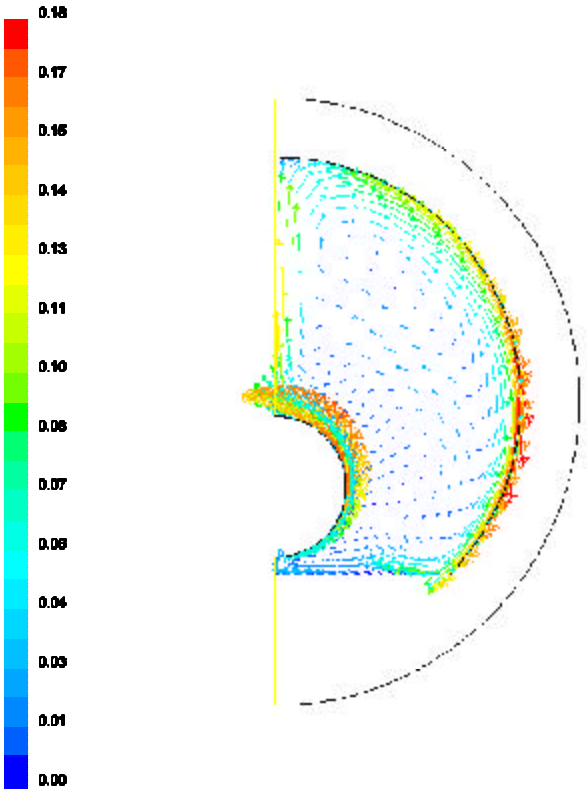

Figure 11. Velocity Vectors (m/s) at Steady State for the 267.2 W Case (44%-scale without Drip Shield).

The gap width Rayleigh numbers are greater for the geometries without drip shields (e.g., both L and the temperature difference across L are larger without the drip shield). Because the characteristic velocity is proportional to the square root of the Rayleigh number ($u_c = \sqrt{gbL\Delta T}$), the CFD simulations without a drip shield result in somewhat larger velocities than geometries with a drip shield. For the 25%-scale simulation, the maximum velocity without drip shield is 0.147 m/s, or about 16% larger than the drip shield case. For the 44%-scale simulation, the without drip shield maximum velocity of 0.19 m/s is about 12% larger than the drip shield case. The maximum heat source temperatures are greater for the drip shield cases, by about 5.5°C and 6.5°C for the 25%-scale and 44%-scale, respectively. The temperature behavior is a function of both fluid flow and thermal radiation. For the same heat flux, a higher Rayleigh number (as in the no drip shield simulations) results in a lower heat source temperature (and a slightly higher inside surface concrete temperature). However, the primary difference between these cases is due to thermal radiation heat transfer. The drip shield effectively behaves as a radiation shield. For the same heat transfer rate, additional surface and geometric resistances attributable to the drip shield surface radiative properties result in higher heat source temperatures. This is illustrated in the figures as well as in Table 5.

As previously indicated, both thermal radiation and convection heat transfer are included in the CFD models. The relative heat transfer rates between thermal radiation and convection (and conduction) heat transfer are given in Table 6 (without drip shield) and 7 (with drip shield). The sum of convection and conduction heat transfer is computed with equation (6):

$$Q_c = Q_t - Q_r \tag{6}$$

Table 6. Relative Heat Transfer Rates for the Cases Without Drip Shield

Case	Heat Source (W)		Concrete (W)		Invert (W)	
	Total	Rad only	Total	Rad only	Total	Rad only
25%-scale, No drip shield, Variable spacing and power	33.41	26.86	-32.40	-24.25	-1.01	-2.61
25%-scale, No drip shield, Uniform spacing and power	15.89	13.02	-15.38	-11.79	-0.50	-1.23
44%-scale, No drip shield, Variable spacing and power	58.86	48.30	-57.51	-44.07	-1.33	-4.23
44%-scale, No drip shield, Uniform spacing and power	27.97	23.38	-27.31	-21.36	-0.66	-2.01

Table 7. Relative Heat Transfer Rates for the Cases With Drip Shield

Case	Heat Source (W)		Drip Shield (Inside) (W)		Drip Shield (Outside) (W)		Inside Invert (W)		Outside Invert (W)		Concrete (W)	
	Total	Rad only	Total	Rad only	Total	Rad only	Total	Rad only	Total	Rad only	Total	Rad only
25%-scale, Variable spacing and power	33.41	27.34	-32.40	-24.56	32.40	25.74	-1.01	-2.78	-0.32	-0.71	-32.08	-25.03
25%-scale, Uniform spacing and power	15.89	13.14	-15.37	-11.81	15.37	12.44	-0.51	-1.33	-0.15	-0.32	-15.22	-12.11
44%-scale, Variable spacing and power	58.86	49.73	-57.73	-45.34	57.73	46.98	-1.11	-4.38	-0.49	-1.27	-57.22	-45.71
44%-scale, Uniform spacing and power	27.97	23.83	-27.39	-21.74	27.39	22.68	-0.57	-2.09	-0.23	-0.57	-27.14	-22.10

From Table 6 and 7 it is noted that thermal radiation accounts for about 80% of the total heat transfer to or from a particular surface in the YMP enclosures. The exception to this is the invert floor. In this case, there is considerable cooling (by convection and conduction) of the invert floor to the nearby surrounding fluid.

Although the 2-D CFD simulations provide a working baseline for the temperature and flow conditions for both natural convection tests, three-dimensional CFD simulations (with included power variations from heat source to heat source and heat source size variability) will better

demonstrate interactions between heat sources with specified separation distances and variable diameters.

3.7.1 Grid Independence Study

Resolution of the wall boundary layers at the eccentric position associated with the grid in Figure 2 is shown in Figure 12 for the 86.2 W case. A plot of the vertical velocity illustrates the change in velocity occurring within the near-wall (boundary layer) region. From the figure it is noted that the near-wall region is resolved such that it captures the changes in velocity due to the presence of the wall and subsequent fluid viscosity effects. Treatment of the near-wall region is also important to the turbulence quantities solved in the flow domain. Of particular importance to the turbulence model is the location of the first computational cell from the wall. For the two-layer zonal model (e.g., the near-wall treatment) specified in the RNG k-ε turbulence model applied in the simulations, FLUENT recommends a wall y^+ value (the distance from the wall nondimensionalized by boundary layer and fluid property variables) of approximately 1 or less. Figure 13 illustrates that the wall y^+ values associated with the grid shown in Figure 2 for the 86.2 W case are all less than 1. A wall y^+ of about 1 ensures that the turbulence model is correctly applied in the viscous sublayer adjacent to the wall. The curves in Figure 13 indicate each of the walls in the CFD simulations. Similar results for vertical velocity and wall y^+ have been obtained for the no drip shield cases and for the 44%-scale CFD simulations. In that case, the wall boundary layers are adequately resolved and the y^+ values are approximately 1 (maximum of about 1.6 on the invert floor outside the drip shield for the 267.2 W case) or less for each of the component walls.

Figure 13 indicates that the wall y^+ values are indeed in the acceptable range for the chosen near-wall treatment. However, a grid independence study is also required to determine if the computational grid itself influences the final outcome of the solution.

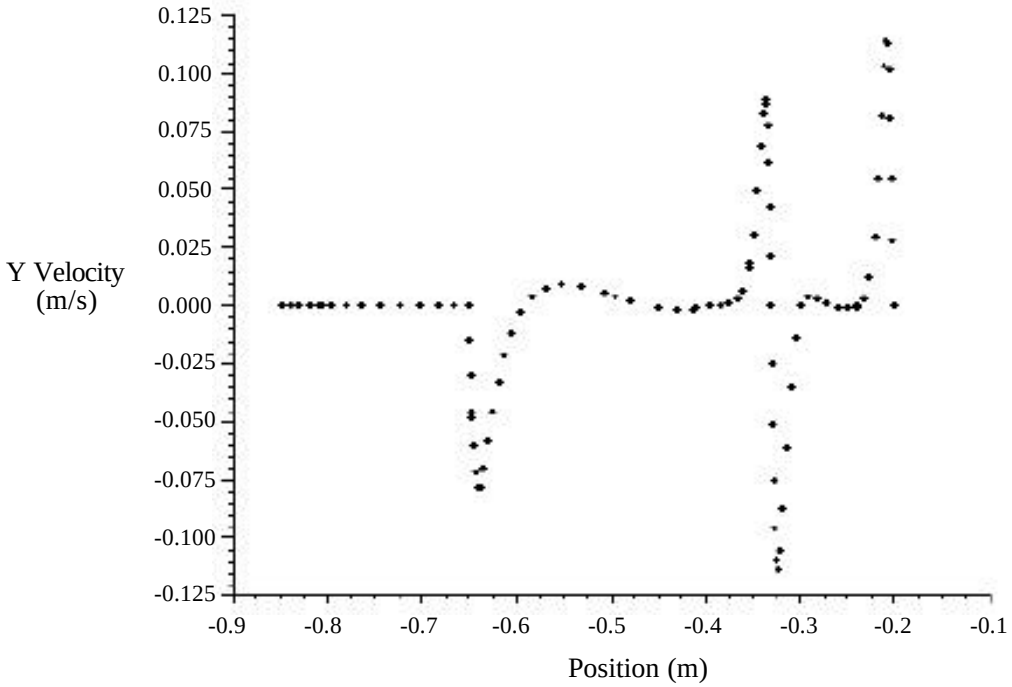

Figure 12. Vertical (or Y) Velocity Profile at the Eccentric Position Shown in Figure 2.

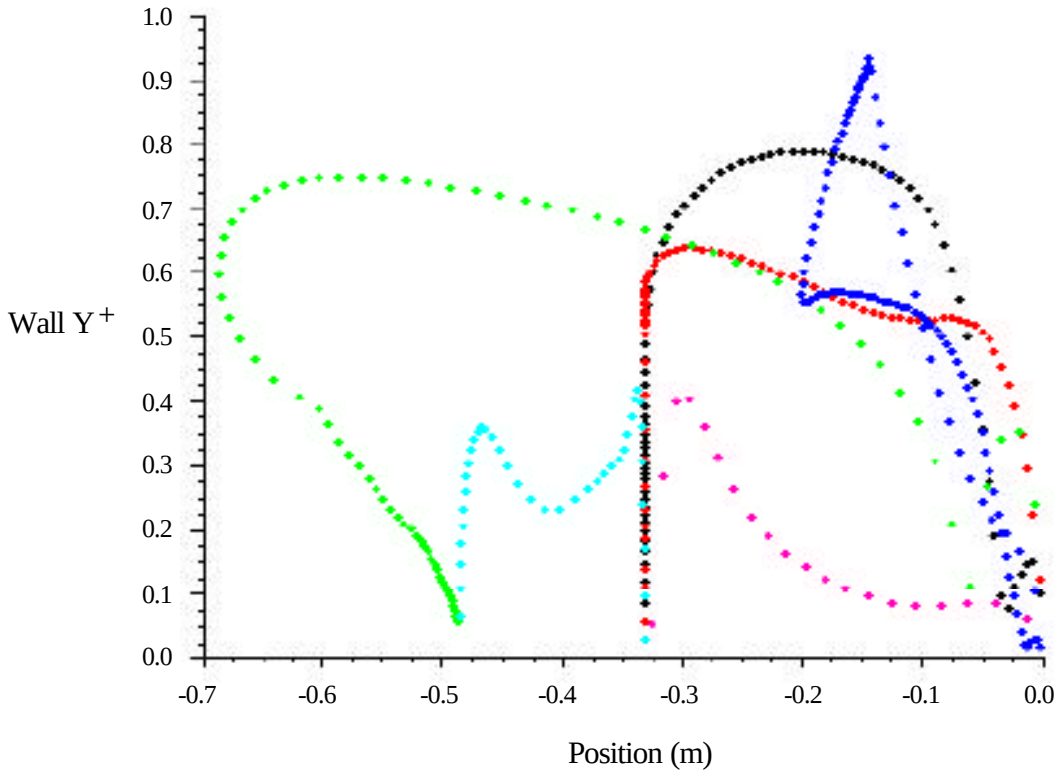

Figure 13. Wall y^+ Values.

A grid independence study is performed for the 86.2 W, 25%-scale, CFD simulation without a drip shield. The working grid for this CFD model had 6143 cells. In order to determine if a grid independent solution was obtained, the geometry was further refined to contain 15,767 cells. All other specifications and inputs remaining the same, temperatures and fluid velocities are assessed to determine if the grid specifications influenced the final outcome. Table 8 provides the temperature comparison.

Table 8. Grid Independence for Temperatures and Velocity

Component Temperature (K) or Maximum Velocity (m/s)	6143 Cells	15,767 Cells	% change
Maximum Heat Source	320.7	320.8	-0.03
Average Heat Source	318.6	318.6	0
Average Invert	314.1	314.1	0
Average Concrete	311.2	311.2	0
Maximum velocity	0.142	0.142	0

Based on Table 8, the grid effects on temperature predictions are minor. A check on the maximum velocity magnitude indicates that the coarse grid is identical to the fine grid. A plot of the vertical velocity through the eccentric position is given in Figure 14 for the coarse and refined grids. The differences in fluid velocities are attributed either to the level of convergence attained with respect to the reduction of equation residuals or the overall density of computational cells. Either way, the comparison between grids is good.

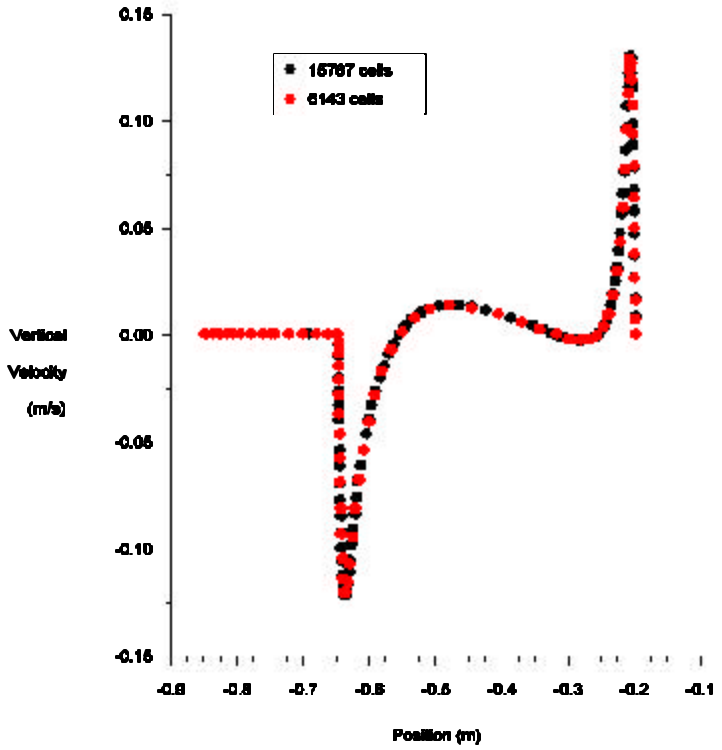

Figure 14. Vertical Velocity Through the Eccentric Position of the 25%-Scale Test.

The velocity profiles (at this specific location) are very similar. Based on this analysis it is noted that the coarse grid does very well in its temperature and velocity predictions. Each of the remaining grids contain more cells than the grid selected in this grid independence study. The 25%-scale without and with drip shield grids contained 6143 and 8145 computational cells, respectively. The 44%-scale without and with drip shield contained 7276 and 9001 computational cells, respectively. Therefore, the CFD simulation results for each test case are considered reasonable based on the grid independence study described above.

4 Discussion

The maximum heat source temperatures ranged from 37 to 50°C without a drip shield and from 40 to 56°C with a drip shield. The CFD model analyses of the experimental test set-ups for natural convection heat transfer was limited to two dimensions. For variable heat source power outputs and separation distances, the application of a two dimensional CFD model to a three-dimensional problem will result in higher predicted temperatures for the high power sources since axial heat flow (by convection and thermal radiation) to cooler locations in the actual experimental apparatus is not allowed in the two-dimensional models. This is especially true of the 86.2 W and 267.2 W cases for the 25%-scale and 44%-scale geometries, respectively. Subsequently, in these non-uniform cases, the maximum heat source temperature predictions

from the two-dimensional models for both with and without drip shield configurations may be overestimated by as much as 25%. The 41 W and 127 W internal heating cases are representative of both uniform heating and spacing configurations. Therefore, the two-dimensional temperature predictions for the uniform spacing and power cases (25%-scale and 44%-scale) should be similar to a three-dimensional representation of these cases.

5 References

Bishop, E.H. 1988. "Heat Transfer by Natural Convection of Helium Between Horizontal Isothermal Concentric Cylinders at Cryogenic Temperature." *Journal of Heat Transfer, 111*, 109-115.

Bishop, E.H., Carley C.T., and Powe, R.E. 1968. "Natural Convective Oscillatory Flow in Cylindrical Annuli." *International Journal of Heat and Mass Transfer,* Vol. 11, 1741-1752. Pergamon Press.

Char, M-I. and Hsu, Y-H. 1998. "Comparative Analysis of Linear and Nonlinear Low-Reynolds Number Eddy Viscosity Models to Turbulent Natural Convection in Horizontal Cylindrical Annuli." *Numerical Heat Transfer, Part A*, (33), 191-206. Washington, DC, Taylor & Francis.

Desai, C. P. and Vafai, K. 1994. "An Investigation and Comparative Analysis of Two- and Three-Dimensional Turbulent Natural Convection in a Horizontal Annulus." *International Journal of Heat and Mass Transfer, 37*, (16), 2475-2504. New York, New York: Pergamon Press.

Farouk, B. and Guceri, S.I. 1982. "Laminar and Turbulent Natural Convection in the Annulus Between Horizontal Concentric Cylinders." *Journal of Heat Transfer*, *104*, (4), 631-636. New York, New York: American Society of Mechanical Engineers.

Fluent Incorporated. 2001. Fluent 6 User's Guide. Volumes 1 to 5. Lebanon, New Hampshire: Fluent Incorporated.

Francis, N.D., Itamura, M.T., Webb, S.W., and James, D.L. 2002. "CFD Calculation of Internal Natural Convection in the Annulus between Horizontal Concentric Cylinders." SAND2002-3132, Sandia National Laboratories, Albuquerque, New Mexico.

Francis, N.D., Webb, S.W., Itamura, M.T., and James, D.L. 2003. "CFD Modeling of Natural Convection Heat Transfer and Fluid Flow in Yucca Mountain Project (YMP) Enclosures." SAND2002-4179, Sandia National Laboratories, Albuquerque, New Mexico.

Fusegi, T. and Farouk, B. 1986. "A Three Dimensional Study of Natural Convection in the Annulus Between Horizontal Concentric Cylinders." *Heat Transfer 1986, Proceedings of The Eighth International Heat Transfer Conference*. C.L. Tien, V.P. Carey, and J.K. Ferrell. 4, 1575-1580. Hemisphere Publishing Corporation.

Incropera, F.P. and DeWitt, D.P. 1990. *Fundamentals of Heat and Mass Transfer*. 3rd Edition. New York, New York: John Wiley & Sons.

Kalia, H.N. 2001. "Guidance for the Implementation of Convection Test." Memorandum from H.N. Kalia (BSC) to Distribution, June 22, 2001, PROJ.06/01.053, with enclosure (MOL.20010719.0155).

Kuehn, T. H. 1976. *Natural Convection Heat Transfer from a Horizontal Circular Cylinder to a Surrounding Cylindrical Enclosure*. Ph.D. Dissertation. Ann Arbor, Michigan: University Microfilms International/University of Minnesota.

Kuehn, T.H. and Goldstein, R.J. 1976a. "An Experimental and Theoretical Study of Natural Convection in the Annulus Between Horizontal Concentric Cylinders." *Journal of Fluid Mechanics, 74*, (part 4), 695-719

Kuehn, T.H. and Goldstein, R.J. 1976b. "Correlating Equations for Natural Convection Heat Transfer Between Horizontal Circular Cylinders." *International Journal of Heat and Mass Transfer, 19*, (10), 1127-1134. New York, New York: Pergamon Press.

Kuehn, T.H. and Goldstein, R.J. 1978. "An Experimental Study of Natural Convection Heat Transfer in Concentric and Eccentric Horizontal Cylindrical Annuli." *Journal of Heat Transfer, Transactions of the ASME, 100*, ([4]), 635-640. [New York, New York: American Society of Mechanical Engineers].

Lis, J. 1966. "Experimental Investigation of Natural Convection Heat Transfer in Simple and Obstructed Horizontal Annuli." *Third International Heat Transfer Conference, 2*, (2), 196-204

McLeod, A.E. and Bishop, E.H. 1989. "Turbulent Natural Convection of Gases in Horizontal Cylindrical Annuli at Cryogenic Temperatures." *International Journal of Heat and Mass Transfer, 32*, (10), 1967-1978. New York, New York: Pergamon Press.

Natural Convection Test Assembly and Fabrication Detail Drawings, 2001. (MOL.20011206.0093).

Raithby, G.D. and Hollands, K.G.T. 1975. "A General Method of Obtaining Approximate Solutions to Laminar and Turbulent Free Convection Problems." In *Advances in Heat Transfer*, 11, 265-315 of Advances in Heat Transfer. New York, New York: Academic Press.

Sanchez, A. and Howard, C. 2003. “Test Report for: Scaled Natural Convection Tests.” ANL-EBS-MD-000065 REV 00. Bechtel SAIC Company, LLC. Las Vegas, Nevada.

Vafai, K., Desai, C.P., Iyer, S.V. and Dyko, M.P. 1997. "Buoyancy Induced Convection in a Narrow Open-Ended Annulus." *Journal of Heat Transfer, 119,* (3), 483-494. New York, New York: The American Society of Mechanical Engineers.

Webb, S.W., Francis, N.D., Dunn, S.D., Itamura, M.T., and James, D.L. 2003. "Thermally-Induced Natural Convection Effects in Yucca Mountain Drifts." *Journal of Contaminant Hydrology*. Vol. 62-63., pp. 713-730.

Appendix A

Hand Calculation for Horizontal Concentric Cylinders

Reference to Francis et al., (2003), indicates that both tests probably exhibit turbulent flow behavior. In order to determine if the natural convection test operating conditions are turbulent, hand calculations are performed for an idealized geometry (concentric cylinders) that is similar to the test geometries. This calculation provides an idea of the temperature difference across the annulus so that a gap-width Rayleigh number can be estimated. With the Rayleigh number, a determination can be made as to whether the internal flow conditions are turbulent or laminar. Turbulent flow conditions in the annulus are expected for a gap-width Rayleigh number larger than about $1x10^6$ (Kuehn and Goldstein, 1978; Desai and Vafai, 1994; Char and Hsu, 1998).

Using the dimensions described in Table 2, an *idealized* test geometry of concentric cylinders (no drip shield or invert) is used to establish an estimate for the temperature difference across the annulus. An estimate of the temperature difference between surfaces (insulation and inside concrete pipe) can be obtained by applying a steady state energy balance through a cross-section of the test. Using the thermal properties in Table 3 for the introduced materials and Equations 14 – 22 in Francis et al., (2002), to compute the effective thermal conductivity for natural convection inside a concentric annulus, the energy balance takes the following form after estimating the interior concrete pipe surface temperature for the 44%-scale test. A steady state energy balance provides the necessary relationship between the heat transfer and the temperature (Incropera and DeWitt, 1990):

$$T_o = Q\left[\frac{\ln\frac{r_c}{r_o}}{2\pi k_c l} + \frac{\ln\frac{r_{in}}{r_c}}{2\pi k_{in} l}\right] + T_\infty \qquad \text{(A-1)}$$

where the radii are r_{in} (= 1.52 m), r_c (= 1.47 m), and r_o (= 1.22 m), the thermal conductivities are k_{in} (= 0.07 W/m-K), k_c (= 2.75 W/m-K), the length is l (2.27 m for the 44%-scale test and 1.29 m for the 25%-scale test), the heat transfer rate is Q (267.2 W), and the uniform exterior temperature is $T_¥$ (300 K). Evaluation of equation (A-1) gives an estimated (inside) concrete pipe temperature of T_o = 310.2 K. Performing an energy balance inside the annulus provides an estimate for the heat source surface temperature. Including both natural convection and thermal radiation heat transfer, a derived steady state energy balance takes the following form (Incropera and Dewitt, 1990):

$$Q = \frac{\sigma A_i\left(T_i^4 - T_o^4\right)}{1/\varepsilon_i + \frac{1-\varepsilon_o}{\varepsilon_o}\left(\frac{r_i}{r_o}\right)} + \frac{2\pi l k_{enc}\left(T_i - T_o\right)}{\ln\frac{r_o}{r_i}} \qquad \text{(A-2)}$$

where the radius is r_i (= 0.35 m), the emissivities are ε_i (= 0.97) and ε_o (= 0.987), the Stefan-

Boltzmann constant is s (= $5.67x10^{-8}$ W/m^2-K^4), and the surface area is $A_i = 2\pi r_i l$. Equation (A-2) contains two unknowns, the heat source temperature, T_i, and the effective thermal conductivity (k_{enc}) for natural convection in the concentric annulus. Therefore, a heat source temperature must initially be assumed so that an effective thermal conductivity can be calculated using equations (14 – 22 in Francis et al., 2002). Now, with a computed $k_{enc,}$ equation (A-2) is used to update the heat source temperature and the procedure is repeated until T_i has converged. Using an initial guess for T_i as 325 K, equations (14 – 22 in Francis et al., 2002) are evaluated for an equivalent conductivity (k_{eq}) of 37 and a bulk fluid temperature ($\overline{T}_B$) of 40.74°C. Using the equivalent conductivity and the bulk temperature to compute the thermal conductivity of air, an equivalent thermal conductivity for annulus natural convection is computed from equation (A-3)

$$k_{eq} = \frac{k_{enc}}{k_a} \tag{A-3}$$

as k_{enc} (= 1 W/m-K). This can now be substituted into equation (A-2) to compute a new T_i. Solving a fourth order polynomial for T_i gives a new estimate for the heat source temperature as 316.1336 K. Repeating this iterative process three more times results in a converged heat source temperature of, T_i (= 316.5 K). With an estimate of the temperature difference across the annulus, a determination of the Rayleigh number based on gap width can be made.

An estimate of the Rayleigh number based on gap width, L ($r_o - r_i$ = 1.22 – 0.35 m = 0.87 m), is computed (for the 44%-scale test) at a film temperature of 314 K as $3x10^8$. This Rayleigh number is greater than 10^6 which implies turbulent flow conditions. A similar energy balance calculation is performed for the 25%-scale test. For a temperature difference of approximately 6.1°C (315.8 – 309.7°C), the resulting gap-width Rayleigh number (Ra_L) is about $5x10^7$. This Rayleigh number also represents turbulent flow conditions in regions of the annulus.

For the case of an idealized drip shield in place, an estimate of the Rayleigh number underneath the drip shield is required to assess the flow conditions there. For idealized gap widths of 0.16 m (L = 0.51 m – 0.35 m) and 0.13 m (L = 0.33 m – 0.2 m) between the heat source and the drip shield for the 44%-scale and 25%-scale tests respectively, the minimum temperature difference for turbulent flow conditions is about 3°C – 6°C.

DISTRIBUTION

External

Sandra Dalvit-Dunn
Science Engineering Associates
3203 Richards Lane
Santa Fe, NM 87505

John Del Mar
Science Engineering Associates
3203 Richards Lane
Santa Fe, NM 87505

Universities

Darryl James (2)
Texas Tech University
Department of Mechanical Engineering
Box 41021
Lubbock, TX 79409-1021

Internal

MS	Org.	
0706	6113	R. E. Finley
0719	6131	S. M. Howarth
0719	6131	S. W. Webb (5)
0735	6115	C. K. Ho
0750	6116	D. J. Borns
0751	6117	L. S. Costin
0751	6117	S. R. Sobolik
0776	6852	T. Hadgu
0776	6852	M. T. Itamura (5)
0776	6852	H. N. Jow
0776	6852	K. M. Knowles
0776	6852	A. W. Reed
0778	6851	R. L. Jarek
0778	6851	C. F. Jove-Colon
0778	6851	R. J. MacKinnon
0836	9116	N. D. Francis (10)
0836	9116	E. S. Hertel, Jr.
1399	6850	A. S. Orrell
1399	6855	C. L. Howard
0731	4415	NWM Library (2)
9018	8945-1	Central Technical Files
0899	9616	Technical Library (2)
0612	9612	Review and Approval Desk, For DOE/OSTI (1)